

# Distorted H I Gas in the Widely Separated LIRG Arp 256

Jacqueline Chen<sup>1,2</sup>

jchen@oddjob.uchicago.edu

K. Y. Lo<sup>1</sup>

kyl@asiaa.sinica.edu.tw

Robert A. Gruendl<sup>3</sup>

gruendl@astro.uiuc.edu

Miao-Ling Peng<sup>4</sup>

and

Yu Gao<sup>5</sup>

gao@ipac.caltech.edu

Received \_\_\_\_\_; accepted \_\_\_\_\_

---

<sup>1</sup>Institute of Astronomy and Astrophysics (ASIAA), Academia Sinica, P.O. Box 23-141, Taipei 106, Taiwan

<sup>2</sup>Department of Astronomy & Astrophysics, University of Chicago, 5640 S. Ellis Ave., Chicago, IL 60637

<sup>3</sup>Laboratory for Astronomical Imaging, Department of Astronomy, University of Illinois, 1002 W. Green Street, Urbana, IL 61801

<sup>4</sup>Department of Earth Sciences, National Taiwan Normal University, Taipei, Taiwan

<sup>5</sup>IPAC, MS 100-22, Caltech, 770 S. Wilson Ave., Pasadena, CA 91125

## ABSTRACT

We present new interferometric H I and CO ( $J = 1 \rightarrow 0$ ) observations of the luminous infrared source, Arp 256. Arp 256 consists of two spiral galaxies in an early stage of merging, with a projected nuclear separation of 29 kpc ( $54''$ ) and an infrared luminosity of  $2.0 \times 10^{11} L_{\odot}$ . Despite the large separation of the galaxies' nuclei and mildly disrupted stellar components, the H I disks are found to be strongly disrupted, and the southern galaxy in Arp 256 shows an elevated star formation efficiency, which is consistent with a nuclear starburst. Both of these results run contrary to expectations, posing interesting questions on the physical mechanisms involved in stimulating star formation during an interaction.

*Subject headings:* galaxies: individual (Arp 256) – galaxies: interactions – galaxies: kinematics and dynamics – galaxies: starburst

## 1. Introduction

Luminous infrared galaxies (LIRGs) are galaxies with  $L_{\text{IR}} \gtrsim 10^{11} L_{\odot}$  and in which most of the bolometric luminosity is emitted in the infrared (see Sanders & Mirabel (1996) for a review). In addition, they are often found in interacting or merging systems – with a frequency ranging from  $\sim 10\%$  at  $L_{\text{IR}} = 10^{10.5} - 10^{11} L_{\odot}$  to  $\sim 100\%$  at  $L_{\text{IR}} > 10^{12} L_{\odot}$  – and are rich in molecular gas (Sanders et al. 1991; Solomon et al. 1992, 1997). A majority of interacting systems, however, are not LIRGs, so interactions are unlikely to be the sole sufficient condition for explaining LIRGs (Keel et al. 1985; Bushouse 1986; Kennicutt et al. 1987).

Numerical simulations of interacting systems suggest that LIRGs might be powered by nuclear starbursts. Starbursts are triggered as tidal interaction strips angular momentum

from molecular gas in the galaxies and gas clouds are drawn into the circumnuclear region during the late stages of interaction (Mihos & Hernquist 1996; Barnes & Hernquist 1996). This scenario does not explain off-nuclear starbursts and gas concentrations observed in some systems (Stanford et al. 1990; Sargent & Scoville 1991; Mirabel et al. 1998), although some simulations do show enhanced extra-nuclear star formation (e.g., Fig. 13, Mihos & Hernquist (1996)). In addition, numerical simulations do not necessarily reflect real star formation processes, since star formation is modeled, by the Schmidt Law, as a function of gas density only. Previous observational work on LIRGs have found nuclear starbursts and gas concentrations consistent with the numerical results, but these studies generally focused on late-stage mergers and ultraluminous infrared galaxies (ULIRGs), which lack the initial condition information that would be useful in comparisons to simulations (Keel et al. 1985; Sanders & Mirabel 1996).

Few studies have explored mergers of gas-rich galaxies over the entire merger sequence. Hibbard & van Gorkom (1996) studied a range of phases in the merger sequence in the H I, H II, and  $R$ -bands for a small sample of galaxies. They suggest that H I disks should become more disrupted as the merger progresses, from  $\sim 60\%$  of the  $M_{\text{HI}}$  being found in the main disks and bulges of each system at an early stage to near  $0\%$ , late in the merger sequence. In addition, Gao & Solomon (1999) have shown that star formation efficiency ( $\text{SFE} = L_{\text{IR}}/M_{\text{H}_2}$ ) increases as separation between interacting galaxy pairs decreases. In general, these results, as well as other observational results and numerical simulations suggest that the starburst phase of interacting galaxies occurs at a late stage in the interaction and is confined to the central kpc.

Arp 256 is composed of two galaxies separated by  $\sim 54''$ . Arp 256 N (north) is a SB(s)c galaxy, while Arp 256 S (south) is a SB(s)b galaxy. At a redshift of  $z = 0.02715$ ,  $cz = 8140$  km s $^{-1}$ , their distance has been calculated at 98.1 Mpc ( $H_0=75$  km s $^{-1}$  Mpc $^{-1}$ ) with a

projected nuclear separation of 29 kpc (Condon et al. 1990; Surace et al. 1993). The IR luminosity based on IRAS observations is  $2.0 \times 10^{11} L_{\odot}$ , but neither galaxy is known to have AGN activity and both show H II region-like spectra (Veilleux et al. 1995). The relatively large separation between the galaxies in Arp 256 suggests that the system is in an early phase of merging and, thus, is of interest as an observational example of a LIRG in the early stages of the formation process.

## 2. Observations and Data Reduction

Table 1 summarizes the details of all the observations. H I 21 cm observations of Arp 256 were conducted with the Very Large Array (VLA) in the 'C' configuration on 1998 December 14. The time on source was nearly 7 hours, and the half-power beamwidth of  $\sim 32'$  was centered between the two galaxies and fully covered all the emission with a velocity bandwidth of 63 channels of  $21.75 \text{ km s}^{-1}$  each. The observing frequency was 1.3826 GHz, corresponding to  $8159 \text{ km s}^{-1}$  in the optical definition of velocity with respect to the Local Standard of Rest. The AIPS software package was used for the calibration and data reduction. The data was carefully flagged and two calibration sources, quasars 3C48 (IAU name: 0137+331) and 0022+002, were used to derive the antenna-based gain and the bandpass solutions. The continuum was estimated from the line-free channels (channels 1-24 and 45-63, velocity ranges  $8833 - 8333$  and  $7876 - 7485 \text{ km s}^{-1}$ ) and subtracted in the  $u - v$  plane with UVLIN to result in a data cube with only H I emission. H I emission is clearly detected in the velocity range  $8290 - 7963 \text{ km s}^{-1}$  (channels 26-41), a velocity linewidth of  $370 \text{ km s}^{-1}$ . Two image maps were made from this data cube. One resultant map uses a synthesized beam of  $19''.2 \times 14''.8$  and a ROBUST = 0 weight function to achieve  $0.38 \text{ mJy beam}^{-1}$  rms noise level. An additional, “naturally” weighted map, with synthesized beam of  $24''.8 \times 18''.7$ , was made and used to construct a velocity contour map (see Figure 5).

A radio continuum image was extracted from the the emission-free channels (channels 3-22, 43-61, velocity ranges 8790 - 8377 and 7920 - 7528 km s<sup>-1</sup>) of the H I dataset. A ROBUST=-5, “uniform” weight function was used in order to maximize the resolution of the image, resulting in a 17''.7 × 13''.5 synthesized beam and 0.61 mJy beam<sup>-1</sup> rms noise level.

CO ( $J = 1 \rightarrow 0$ ) in Arp 256 was observed in 1998 May and November at the Berkeley-Illinois-Maryland Association (BIMA) 10-element millimeter wave array in the ‘C’ configuration. Arp 256 was observed for 28 minutes, alternated with 6.5 minute observations of the phase and amplitude gain calibrator 0006-063 for a total time on source of 9 hours. Mars and Uranus were observed as flux calibrators. The pointing was centered between the galaxies and the half-power beamwidth of  $\sim 2'$  covered the central 64 kpc. The observing frequency was 112.2204 GHz, corresponding to 8149 km s<sup>-1</sup> in the optical convention. In addition, 78 channels of 19.9 km s<sup>-1</sup> velocity width provided full frequency coverage. Line emission was found in channels 27-48 – velocity range 7890 - 8308 km s<sup>-1</sup> – for a velocity linewidth of 440 km s<sup>-1</sup>. Calibration and data reduction were done with the MIRIAD software package. The resultant map uses a synthesized beam of 11''.5 × 4''.9 and natural weighting to achieve a 0.038 Jy beam<sup>-1</sup> rms noise level.

### 3. Results

#### 3.1. Spatial Distribution of the H I Emission

In Figure 1, the H I column density map is overlaid on a  $J$ -band image of Arp 256 from a mosaic of 52 exposures of 60 seconds each from observations made with the NIRIM camera (Meixner, Young Owl, & Leach 1999) on the Mount Laguna Observatory 1-m telescope. The H I distribution shows a spiral pattern, but, when compared to the near-infrared image,

the H I emission peaks do not correspond to the optical emission peaks of the galaxies. This suggests that the original H I disks associated with the two galaxies have been severely disrupted despite the large separation between the two galaxies. The strong disruption of the H I disks may indicate that the galaxies have passed the period of first closest approach.

The integrated flux measured in the VLA map is  $6.6 \text{ Jy km s}^{-1}$ , which is essentially the same as the single-dish flux of  $6.01 \text{ Jy km s}^{-1}$ , measured by Bushouse (1987). From the integrated flux, the total H I mass can be estimated by

$$M_{\text{HI}}(M_{\odot}) = 2.36 \times 10^5 D^2 \int S dv,$$

where  $D$  is distance in Mpc, and  $\int S dv$  is H I integrated flux in  $\text{Jy km s}^{-1}$  (Roberts 1975). The value of  $\int S dv$  is obtained by summing the flux in the channel maps. The resultant total H I mass is  $1.5 \times 10^{10} M_{\odot}$ .

The H I channel maps and the position-velocity map show at least four distinct gas components (see Figures 2,3): the tail of H I emission extending from the northern arm of Arp 256 N; the central peak of emission between the two galaxies; a small amount of gas that overlaps the optical emission of Arp 256 S on the sky; and the emission peak to the south-west of Arp 256 S. These components have  $\sim 20$ , 30, 5, and 15% of the integrated flux, and therefore of the total H I mass, respectively.

### 3.2. Spatial Distribution of the CO Emission

Figure 1 also shows the integrated CO intensity map overlaid on the optical image. In contrast to the H I distribution, the CO emission associated with Arp 256 S appears unresolved, as well as undisturbed, and well-confined within the circumnuclear regions of the galaxy. No CO emission is detected in the nuclear regions of Arp 256 N, although there is a marginal,  $3\sigma$  detection in the vicinity of the southern major spiral arm. The absence of

detected emission in Arp 256 N is unexpected for a late-type spiral (Sc) galaxy. In general, early-type spirals – Sab and Sb – have a  $M_{\text{H}_2}/M_{\text{HI}}$  ratio around 2 and spiral galaxies later than Sc have a ratio smaller than 1 (Young & Knezek 1989), but the original H I disks of Arp 256 have been disrupted, so this comparison is no longer possible.

We estimate the molecular gas mass from the integrated CO(1-0) flux using the empirical relation (Scoville et al. 1987):

$$M_{\text{H}_2}(M_{\odot}) = 1.18 \times 10^4 D^2 \int S dv,$$

where  $D$  is distance in Mpc and  $\int S dv$  is CO integrated flux in Jy km s<sup>-1</sup>. Here the Galactic conversion factor  $X \equiv N(\text{H}_2)/I_{\text{CO}} = 3.0 \times 10^{20} \text{ cm}^{-2} (\text{K km s}^{-1})^{-1}$  (see Young & Scoville (1991) for a review) is assumed for convenient comparison with previous results. We note that this conversion factor may cause an overestimation of the molecular gas mass if the galaxy is undergoing starbursts (e.g., Maloney & Black (1988); Bryant & Scoville (1999)). The integrated flux of the CO emission associated with the southern nucleus is 42 Jy km s<sup>-1</sup>, resulting in an estimated H<sub>2</sub> mass for the southern nucleus of  $4.8 \times 10^9 M_{\odot}$ . The  $1\sigma$  upper limits to the integrated flux and the  $M_{\text{H}_2}$  for the northern source are 29 Jy km s<sup>-1</sup> and  $3.3 \times 10^9 M_{\odot}$ , respectively, employing the same linewidth as Arp256 S.

### 3.3. Spatial Distribution of the Radio Continuum

A 21 cm radio continuum map was extracted from line-free channels of the VLA H I observations and displayed in Figure 1. A strong, unresolved radio source overlaps the bulge of Arp 256 S. Weaker continuum emission is detected in the direction of Arp 256 N, with a peak over the northern major spiral arm and a weaker peak over the southern major spiral arm (see Figure 4), with the possibility that the radio emission forms a spiral to match the spiral arms of the galaxy. Future observations should include a higher resolution radio map

in order to follow up on this unusual structure.

Measurements of the 20 cm radio continuum flux imply that the radio continuum is emitted almost entirely from the circumnuclear region of Arp 256 S – inside a radius of 2 kpc. Condon et al. (1998) find an integrated flux density of 43.2 mJy at a resolution of 45", while the VLA Faint Images of the Radio Sky at Twenty-Centimeters (FIRST) Survey finds 34.82 mJy within a  $\sim 4''$  beam (White et al. 1997). This corroborates the high level of activity in the southern source as seen in our map and implies the presence of a star forming region or an AGN in Arp 256 S. A closer inspection of the southern galaxy may detect a slight offset between the peak in emission of the radio continuum and the peak in emission of the CO disk. While the radio continuum emission appears to be centered directly on the *J*-band image peak, the CO emission appears slightly to the north-east. This offset, while intriguing, is similar to the pixel size for both the CO map and the *J*-band map and has to be verified by further observations.

### 3.4. Kinematics

Figure 5 shows isovelocity contours from the first moment of the H I data cube. The velocity field appears to have the characteristics of two “spider diagrams” centered at the nuclei of the two galaxies. However, as the spectral lines are not single peaked and the velocity gradients do not follow the major axes of the optical galaxies – as would have been expected for an isolated, rotating, inclined disk – the “spider diagram” features are likely incidental. The systemic velocities of the two galaxies appear very similar,  $\sim 8150 \text{ km s}^{-1}$ , measured via the optical definition with respect to the Local Standard of Rest. It is possible that Arp 256 N has a slightly greater recessional velocity, 8175 compared to  $8125 \text{ km s}^{-1}$  for Arp 256 S. In comparison, heliocentric optical redshifts for the two galaxies show the northern nucleus at  $8193 \text{ km s}^{-1}$  and the southern nucleus at  $8112 \text{ km s}^{-1}$ . In addition,



the CO map for Arp 256 S shows a velocity width of  $300 \text{ km s}^{-1}$ , centered around  $8130 \text{ km s}^{-1}$ , calculated via the optical definition. The H I gas appears to “rotate” about Arp 256 N, from south-south-west to north-east between  $8246$  and  $8050 \text{ km s}^{-1}$ , whereas the H I around Arp 256 S “rotates” from near the galaxy to west-south-west between  $8159$  and  $8007 \text{ km s}^{-1}$ , asymmetric in distribution.

These rotational signatures may be misleading, since, in searching for signatures of rotational motion in smaller slices of the spatial-velocity diagram, it becomes apparent that very little gas can actually be attributed to any particular galaxy. For example, Figures 6 and 7 are spatial velocity diagrams for the two galaxies of Arp 256 separately, summing emission perpendicular to the approximate east-west alignment of the major axes of both galaxies. They clearly show that despite the large amount of H I gas in the system, very little of the original H I disks around Arp 256 N and S remain. The declinations which correspond to the optical bulges of the galaxies appear at approximately the same velocity,  $8115 \text{ km s}^{-1}$ . In addition, the major peaks of emission (offset on the sky from the galaxies) do not exhibit normal rotational motion and appear essentially at one velocity. At lower velocities, the northernmost peak of emission appears at  $8070 \text{ km s}^{-1}$ , while the southernmost peak is at  $8030 \text{ km s}^{-1}$ . At higher velocities, the strongest peak of emission, between the two galaxies, appears at two distinct velocities,  $8160$  and  $8250 \text{ km s}^{-1}$ .

Any attempt to synthesize the kinematic data into an orbital geometry for the system can be only partly successful, as we remain burdened with too many degrees of freedom. Given the lack of strong tidal tails and the strong disruption of the H I disks, it is likely that at least one of the spin vectors of the galaxies is retrograde with respect to the orbital angular momentum vector and a prograde-prograde configuration is unlikely (Mihos & Hernquist 1996). The velocity contours show that the direction of the gradient in the two galaxies is in opposite directions along an east-west axis. However, as the galaxies appear to

be at least somewhat face-on with respect to the plane of the sky – Arp 256 S is measured at an inclination of  $48^\circ$  (Bottinelli et al. 1982; Martin et al. 1991) – even this is inconclusive in determining whether the galaxies’ spin axes are aligned or in opposite directions.

#### 4. Discussion

Given the level of activity in the southern galaxy, it is appropriate to ask whether the source is a starburst or an AGN. The answer, however, is difficult to determine definitely. A simple way to distinguish between a nuclear starburst and an AGN would be to resolve the center of the galaxy; a nuclear starburst would be confined to  $\lesssim 1$  kpc of the center, while an AGN would be confined to a much smaller radius. In addition, an offset of the radio continuum emission from the gas that might feed star formation or from starlight could distinguish a starburst from an AGN. Current radio continuum images of Arp 256 S are unable to resolve the center of the galaxy and distinguish between a nuclear starburst or an AGN. They resolve at best to only 1-2 kpc, and the previously noted offset of the CO disk is inconclusive, given the resolution of our images. Starbursts exhibit a strong far-infrared / radio continuum correlation (see Condon, Anderson, & Helou (1991)), which also proves inconclusive in the case of Arp 256, falling within an acceptable range for a starburst, but not ruling out an AGN (Liang 2000). However, previously published data of line ratios taken from optical spectra distinguish between a starburst and an AGN. Veilleux et al. (1995) find, via optical spectra, that both of the galaxies in Arp 256 are H II region-like (not powered by an AGN) and neither LINER nor Seyfert-like. In addition, Bushouse & Werner (1990) find significant  $H\alpha$  emission in the southern nucleus, supporting those results.

The star formation efficiency (SFE) of the galaxies can be estimated by the ratio  $L_{\text{IR}}(8 - 1000\mu\text{m})/M_{\text{H}_2}$ . Given a  $L_{\text{IR}}$  from Carico et al. (1988, 1990) of  $0.87 \times 10^{11} L_\odot$  for the northern source and of  $1.17 \times 10^{11} L_\odot$  for the southern source, the SFE of Arp 256 S

is  $24.4 L_{\odot}/M_{\odot}$ , far higher than the typical SFE of giant molecular clouds in the Milky Way (Scoville & Good 1989,  $\sim 4L_{\odot}/M_{\odot}$ ) and within the 20-100  $L_{\odot}/M_{\odot}$  range for nuclear starburst galaxies (Scoville et al. 1991). The  $L_{\text{IR}}$  given by Carico et al. (1988, 1990), however, is likely to be an underestimate as it is based upon an extrapolation from near-IR measurements and assumptions about the far-infrared ratios. On the other hand, from the radio continuum map, it is clear that  $\sim 75\%$  of the emission is from the southern source. The total IR luminosity detected by IRAS is  $2.0 \times 10^{11} L_{\odot}$ . If we assume that Arp 256 S emits  $\sim 75\%$ , then we estimate a similar SFE for Arp 256 S of  $\sim 30 L_{\odot}/M_{\odot}$ .

It seems likely, then, that there is a starburst in the nuclear regions of Arp 256 S. The infrared luminosity and the molecular gas mass give an estimate of how long it will take for the molecular gas to run out. If we assume the infrared luminosity is entirely due to dust heated by young stars in recent star formation, the star formation rate (SFR) is directly proportional to the infrared luminosity, with a relation of  $\text{SFR} (M_{\odot} \text{ yr}^{-1}) \sim 1 \times 10^{-10} L_{\text{IR}}(L_{\odot})$  for stars with masses greater than  $2 M_{\odot}$  (Gallagher & Hunter 1986). For Arp 256, the estimated star formation rate would be  $11.7 M_{\odot} \text{ yr}^{-1}$ . This rate essentially measures gas depletion, so given the inferred molecular gas mass, the molecular gas will be exhausted in  $\sim 4 \times 10^8 \text{ yr}$ . This timescale is inconsistent with the expectation of a nuclear starburst at a late stage of merging for galaxies with central bulges. Given that Arp 256 is currently in an early-stage of merging associated with the period of first close approach (Mihos & Hernquist 1996), the starburst in Arp 256 S will be exhausted before the late stages of merging.

In comparison to other studies, other discrepancies also arise. Gao & Solomon (1999), in a study of SFE in systems at various stages of interaction, note a correlation between SFE and interaction time – the longer the interaction time, the greater the SFE – which supports the standard model of starbursts at late stages of mergers. In comparison to that

study, Arp 256 has the highest SFE for its apparent separation (the measure of interaction time used). The highly disrupted H I disk and the low percentages of flux associated with the optical disks of each galaxy also run contrary to the results of Hibbard & van Gorkom (1996), who find an anti-correlation between the stage of merger and the central H I mass. Other observations, however, find cases of early-stage mergers with possible starbursts (e.g., Wang et al. (2001)).

The lack of detected CO would imply that Arp 256 N has little star formation activity. Veilleux et al. (1995), however, identify the galaxy as H II region-like. In addition, the H $\alpha$ -band images of Arp 256 N of Bushouse & Werner (1990), clearly show a peak of emission in the northern arm but not in its nucleus, nor in the southern arm – where we had a marginal detection of CO and an upper limit of  $M_{\text{H}_2} \lesssim 3.3 \times 10^9 M_{\odot}$ . Our radio continuum map peaks off-nucleus and may possibly overlap the H $\alpha$  peak in the northern arm and is, therefore, consistent with the results of Veilleux et al. (1995).

## 5. Conclusions

From our new observations of H I and CO in Arp 256 we see evidence contradicting the standard model of LIRGs. Despite the large separation between the galaxies and no morphological evidence of interaction that would accompany an intermediate or late stage merger, Arp 256 displays the highly disrupted H I disks and increased SFE commonly associated with a late stage of merging. The interaction history of Arp 256 that has led it to its current set of characteristics, however, are unavailable with current evidence and models, and more study is required of this system and others like it.

We thank S.-W. Lee for assisting in the acquisition of data and D.-C. Kim and D.B. Sanders for the use of the *R*-band image of Arp 256. We are grateful to John Hibbard, the

referee, for critical comments which were very helpful in improving the paper. We would also like to thank W.-H. Wang for his invaluable comments and suggestions. The research has made use of the NASA/IPAC Extragalactic Database (NED) which is operated by the Jet Propulsion Laboratory, California Institute of Technology, under contract with the National Aeronautics and Space Administration. R. A. Gruendl acknowledges support from the Laboratory of Astronomical Imaging, which is funded by the NSF grant AST 99-81363 and by the University of Illinois. M.-L. Peng started the VLA H I data reduction while a summer student at the ASIAA. Research at the ASIAA is supported by the Academia Sinica in Taipei and the National Science Council of Taiwan.

## REFERENCES

- Barnes, J. E., & Hernquist, L. 1996, *ApJ*, 471, 115
- Bottinelli, L., Gouguenheim, L., & Paturel, G. 1982, *A&A*, 113, 61
- Bryant, P. M., & Scoville, N. Z. 1999, *AJ*, 117, 2632
- Bushouse, H. A. 1986, *AJ*, 91, 255
- Bushouse, H. A. 1987, *ApJ*, 320, 49
- Bushouse, H. A., & Werner, M. W. 1990, *ApJ*, 359, 72
- Carico, D. P., Sanders, D. B., Soifer, B. T., Elias, J. H., Matthews, K., & Neugebauer, G. 1988, *AJ*, 95, 356
- Carico, D. P., Sanders, D. B., Soifer, B. T., Matthews, K., & Neugebauer, G. 1990, *AJ*, 100, 70
- Condon, J. J., Helou, G., Sanders, D. B., & Soifer, B. T. 1990, *ApJS*, 73, 359C
- Condon, J. J., Anderson, M. L., & Helou, G. 1991, *ApJ*, 376, 95
- Condon, J. J., Cotton, W. D., Greisen, E. W., Yin, Q. F., Perley, R. A., Taylor, G. B., & Broderick, J. J. 1998, *AJ*, 115, 1693
- Gallagher, J. S., & Hunter, D. A. 1986, in *Conf. Proc. of Star Formation in Galaxies*, Pasadena, ed. C. Lonsdale (Washington, DC: GPO), 167
- Gao, Y., & Solomon, P. M. 1999, *ApJ*, 512, L99
- Hibbard, J. E., & van Gorkom, J. H. 1996, *AJ*, 111, 655
- Keel, W. C., Kennicutt, R. C., Hummel, E., & van der Hulst, J. M. 1985, *AJ*, 90, 708

- Kennicutt, R. C., Keel, W. C., van der Hulst, J. M., & Roettiger, K. A. 1987, *AJ*, 93, 1011
- Liang, M. C. 2000, personal communication.
- Maloney, P., & Black, J. H. 1988, *ApJ*, 325, 389
- Martin, J. M., Bottinelli, L., Dennefeld, M., & Gouguenheim, L. 1991, *A&A*, 245, 393
- Meixner, M., Young Owl, R., & Leach, R. W. 1999, *PASP*, 111, 997
- Mihos, J. C., & Hernquist, L. 1996, *ApJ*, 464, 641
- Mirabel, I. F., Vigroux, L., Charmandaris, V., Sauvage, M., Gallais, P., Tran, D., Cesarsky, C., Madden, S. C., & Duc, P.-A. 1998, *A&A*, 333, L1
- Roberts, M. S. 1975, in *Galaxies and the Universe*, A. Sandage, M. Sandage, & J. Kristian eds. (Chicago: University of Chicago Press) 309
- Sanders, D. B., & Mirabel, I. F. 1996, *ARA&A*, 34, 749
- Sanders, D. B., Scoville, N. Z., & Soifer, B. T. 1991, *ApJ*, 370, 158
- Sargent, A. I., & Scoville, N. Z. 1991, *ApJ*, 366, L1
- Scoville, N. Z., Sargent, A. I., Sanders, D. B., & Soifer, B. T. 1991, *ApJ*, 366, L5
- Scoville, N. Z., & Good, J. 1989, *ApJ*, 339, 140
- Scoville, N. Z., Yun, M. S., Clemens, D. P., Sanders, D. B., & Walker, W. H. 1987, *ApJS*, 63, 821
- Soifer, B. T., Sanders, D. B., Madore, B., Neugebauer, G., Danielson, G. E., Elias, J. H., Lonsdale, C. J., & Rice, W. L. 1987, *ApJ*, 320, 238
- Solomon, P. M., Downes, D., Radford, S. J. E., & Barrett, J. W. 1997, *ApJ*, 478, 144

Solomon, P. M., Downes, D., & Radford, S. J. E. 1992, *ApJ*, 387, L55

Stanford, S. A., Sargent, A. I., Sanders, D. B., & Scoville, N. Z. 1990, *ApJ*, 349, 492

Surace, J. A., Mazzarella, J., Soifer, B. T., & Wehrle, A. E. 1993, *AJ*, 105, 864

Veilleux, S., Kim, D. -C., Sanders, D. B., Mazzarella, J. M., & Soifer, B. T. 1995, *ApJS*, 98,  
171

Wang, W. -H., Lo, K. Y., Gao, Y., Gruendl, R. A., & Hwang, C.Y. 2001, *AJ*, 122, 140

White, R. L., Becker, R. H., Helfand, D. J., & Gregg, M. D. 1997, *ApJ*, 475, 479

Young, J. S., & Scoville, N. Z. 1991, *ARA&A*, 29, 581

Young, J. S., & Knezek, P. M. 1989, *ApJ*, 347, L55



Fig. 1.— Zero moment H I, CO, and radio continuum maps in contours over an optical image. The optical image is a *J*-band image from the Mount Laguna Observatory (MLO) 1-m telescope. The H I emission is marked by the green contours and beamsize indicator. Contour levels are 1, 2, 3, . . . , 12 times  $0.04 \text{ Jy beam}^{-1} \text{ km s}^{-1}$ , which corresponds to a column density of  $1.6 \times 10^{20} \text{ cm}^{-2}$ . The blue contours mark the radio continuum image, in levels of 50, 150, 250, 500, 800, 1100, 1500, 1800, and 2100 times  $0.61 \text{ mJy beam}^{-1}$  ( $1\sigma = 1.54 \text{ K}$ ). The CO emission is given in red contours, also with levels of 3, 5, 7, and 9 times  $3.510 \text{ Jy beam}^{-1} \text{ km s}^{-1}$ , which corresponds to a molecular hydrogen column density of  $1.7 \times 10^{21} \text{ cm}^{-2}$ .

Fig. 2.— ROBUST = 0, uniform weighted H I channel maps, with  $\sigma = 8.3 \text{ mJy beam}^{-1} \text{ km s}^{-1}$  levels overlaid on the MLO *J*-band image. Contours are 2, 4, 6, . . . , 14 times  $\sigma$ . 24-43 of 63 channels are plotted. Each frame is labelled in the top left corner with the line-of-sight velocity in  $\text{km s}^{-1}$ .

Fig. 3.— H I position-velocity ( $p - v$ ) diagram of the summed emission perpendicular to the north-south axis, both in contours and grey-scale. Contour levels are at 10% of the peak at  $51.5 \text{ mJy beam}^{-1}$ . Four emission features are labelled: the tail of HI emission extending from the northern arm (NT), the central peak between the two galaxies (CP), the small amount of gas that overlaps the optical emission of Arp 256 S on the sky (OR), and the emission peak to the southwest of Arp 256 S (SW).

Fig. 4.— Close-up of Figure 1, with only radio continuum contours overlaid on a *R*-band image of Arp 256 N provided by D.B. Sanders and D.-C. Kim. The *R*-band image consists of one 300 second exposure from the Palomar 60-cm telescope. Levels are 40, 75, 110, 140, 170, 205, 250, and 280 times  $0.61 \text{ mJy beam}^{-1}$  ( $1\sigma = 1.54 \text{ K}$ ).

Fig. 5.— H I radial velocity contour and grey-scale map, derived from the naturally weighted

map of Arp 256. Contours are plotted every  $25 \text{ km s}^{-1}$ , the central contours falling at  $8150$  and  $8175 \text{ km s}^{-1}$ .

Fig. 6.— Spatial velocity diagram along the east-west axis of Arp 256 N of emission summed from  $\delta_{2000} = -10^{\circ}22'00''$  to  $\delta_{2000} = -10^{\circ}21'00''$ , approximately perpendicularly to the major axis of the galaxy. Levels are 1, 2, 3, 4, 5 times  $6.0 \text{ Jy beam}^{-1}$ . The nucleus of the optical galaxy falls at  $\alpha_{2000} = 00^{\text{h}}18^{\text{m}}50^{\text{s}}.0$  and  $8115 \text{ km s}^{-1}$ .

Fig. 7.— Spatial velocity diagram along the east-west axis of Arp 256 S of emission summed from  $\delta_{2000} = -10^{\circ}23'12''$  to  $\delta_{2000} = -10^{\circ}22'20''$ , approximately perpendicularly to the major axis of the galaxy. Levels are 1, 2, 3,  $\dots$ , 7 times  $5.6 \text{ Jy beam}^{-1}$ . The nucleus of the optical galaxy falls at  $\alpha_{2000} = 00^{\text{h}}18^{\text{m}}50^{\text{s}}.7$  and  $8115 \text{ km s}^{-1}$ .

Table 1. Observing Parameters

	21 cm Emission	CO ( $J = 1 \rightarrow 0$ )
Telescope	VLA	BIMA
Observation Date	12/98	5/98, 11/98
Velocity Center ( $\text{km s}^{-1}$ ):		
$cz$	7980	7933
Optical Convention	8159 (w.r.t. LSR)	8149
Time on Source (hrs)	7.0	9.1
Number of Channels	63	78
Channel Separation ( $\text{km s}^{-1}$ )	21.75	19.9
Line Velocity Range ( $\text{km s}^{-1}$ )	8290-7963	7890-8308
Integrated Flux ( $\text{Jy km s}^{-1}$ )	6.6	29, 42 <sup>a</sup>
Affiliated Mass ( $10^9 M_{\odot}$ )	15 <sup>b</sup>	3.3, 4.8 <sup>c</sup>

<sup>a</sup>Integrated flux for Arp 256 N and Arp 256 S, respectively, where the value for the northern galaxy is the  $1\sigma$  upper limit.

<sup>b</sup>Total H I mass,  $M_{HI}$ .

<sup>c</sup>Molecular gas mass,  $M_{H_2}$ , for Arp 256 N and Arp 256 S, respectively.

This figure "figure1.gif" is available in "gif" format from:

<http://arxiv.org/ps/astro-ph/0110627v2>

This figure "figure2.gif" is available in "gif" format from:

<http://arxiv.org/ps/astro-ph/0110627v2>

This figure "figure3.gif" is available in "gif" format from:

<http://arxiv.org/ps/astro-ph/0110627v2>

This figure "figure4.gif" is available in "gif" format from:

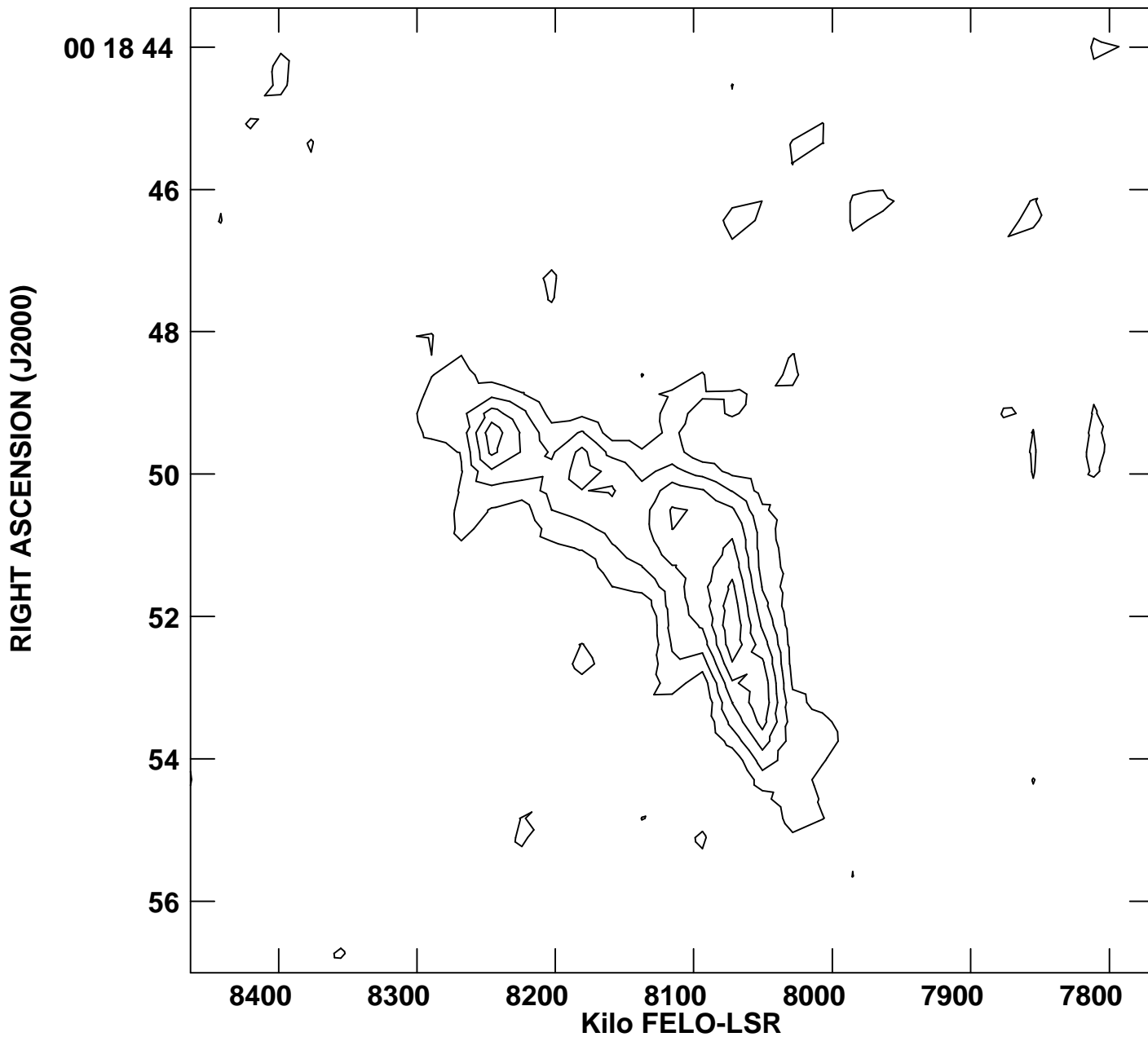
<http://arxiv.org/ps/astro-ph/0110627v2>

This figure "figure5.gif" is available in "gif" format from:

<http://arxiv.org/ps/astro-ph/0110627v2>

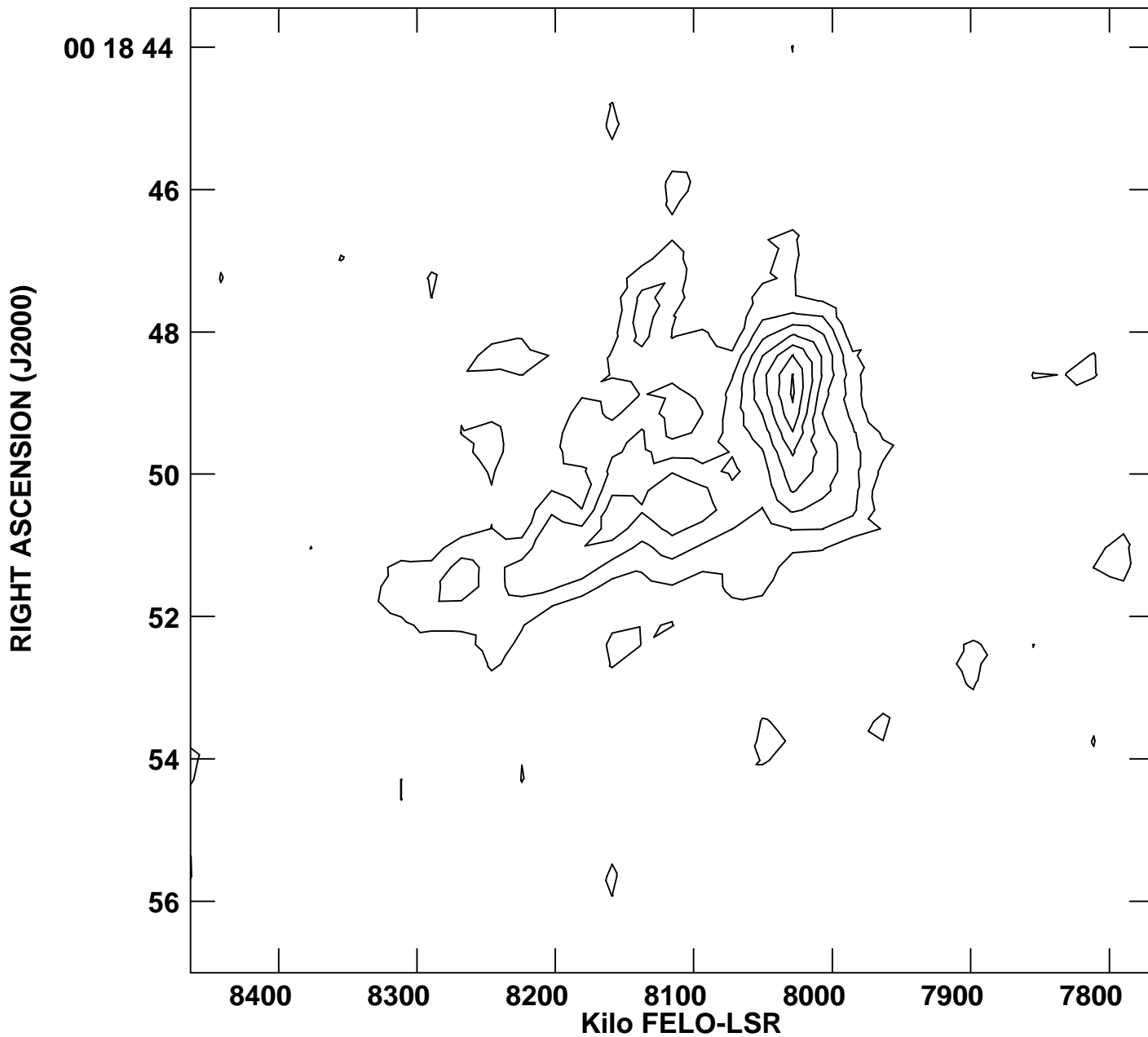


PLot file version 2 created 21-JUL-2000 11:57:28  
ARP256 DEC -10 21 53.10 IPOL ARP256.SQASH.10



Peak flux = 3.5214E-02 JY/BEAM  
Levs = 6.000E-03 \* (1, 2, 3, 4, 5, 6, 7, 8, 9, 10,  
11, 12, 13, 14, 15, 16, 17, 18, 19, 20)

PLot file version 2 created 21-JUL-2000 11:57:05  
ARP256 DEC -10 23 09.10 IPOL ARP256.SQASH.8



Peak flux =  $4.0188\text{E-}02$  JY/BEAM  
Levs =  $5.600\text{E-}03$  \* (1, 2, 3, 4, 5, 6, 7, 8, 9, 10,  
11, 12, 13, 14, 15, 16, 17, 18, 19, 20)